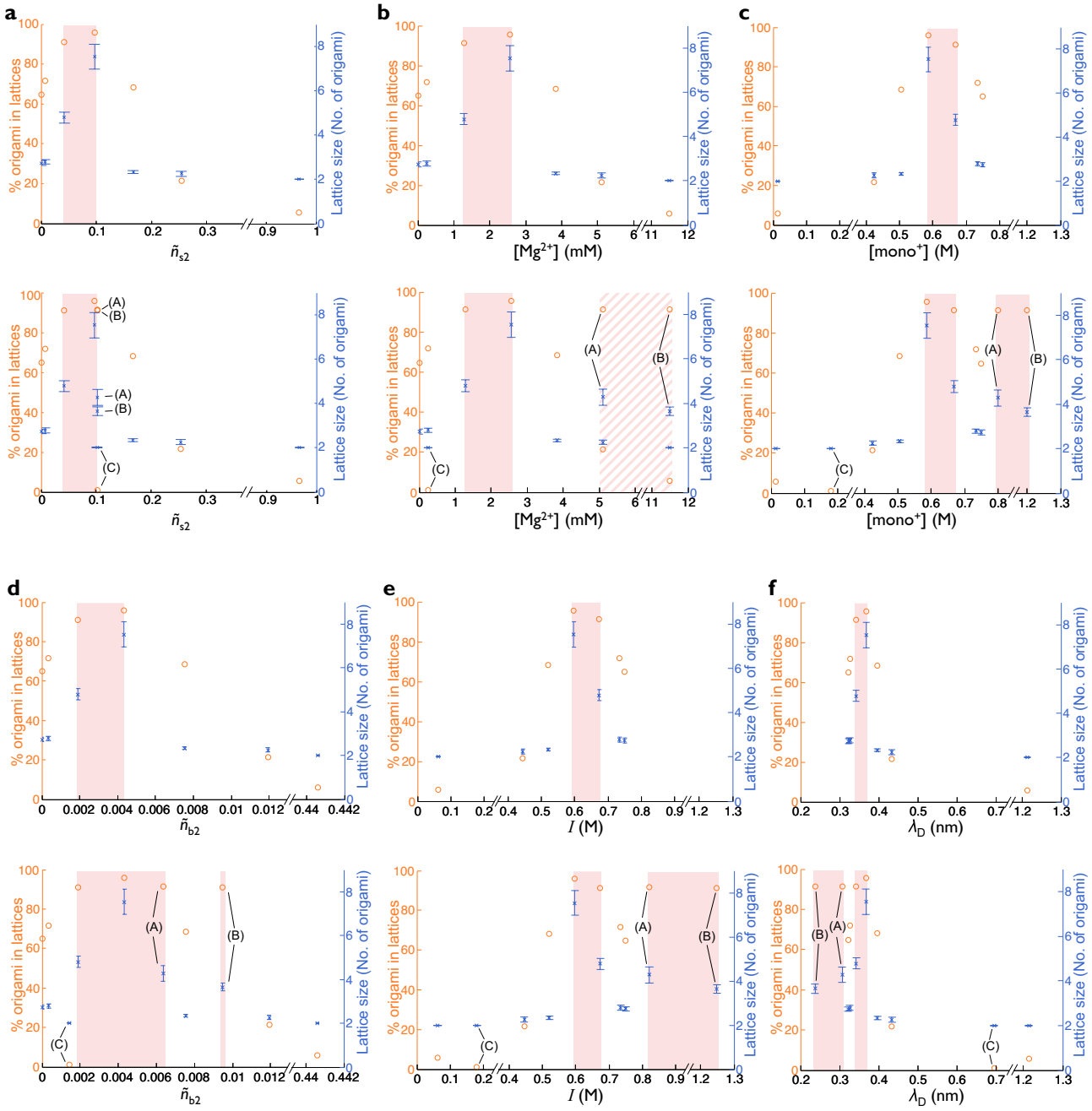

Supplementary Figure 1. Plots illustrating how well different ionic parameters correlate with formation of origami lattices. a-f, (top) Plots of the percentages of origami incorporated into lattices (orange circles), and average lattice sizes (blue Xes) as a function of (**a**) $\tilde{n}_{s2}$, fractional surface density of divalents, (**b**) [Mg^{2+}], bulk magnesium, (**c**) [$mono^{+}$], bulk monovalents (**d**) $\tilde{n}_{b2}$, fractional bulk concentration of divalents (**e**) I, ionic strength and (**f**) λ_D, Debye length. These plots show that any parameter could be used equally well to define a working regime. (pink shaded areas indicating lattice incorporation > 90%). (bottom) For each plot, additional data points for conditions (A), (B), and (C) were added. With the inclusion of conditions (A) and (B) only $\tilde{n}_{s2}$ still gives a continuous working regime. The area with a diagonally striped pattern in the bottom plot in (**b**) indicates that conditions with both excellent (>90%) and poor (20% or less) lattice incorporation rates exist for the same [Mg^{2+}] values. Condition (C) has an extremely low lattice incorporation rate, inconsistent with the working regime for $\tilde{n}_{s2}$, which we attribute to its low ionic strength and high Debye length. Error bars indicate standard error (n = 489, 528, 1133, 1196, 382, 167, 209, in order of the data points from left to right in the top plots of (**a**), (**b**), (**d**), and (**f**), and in reverse order in the top plots of (**c**) and (**e**); n = 495, 396, 210 for conditions (A), (B), and (C), respectively).

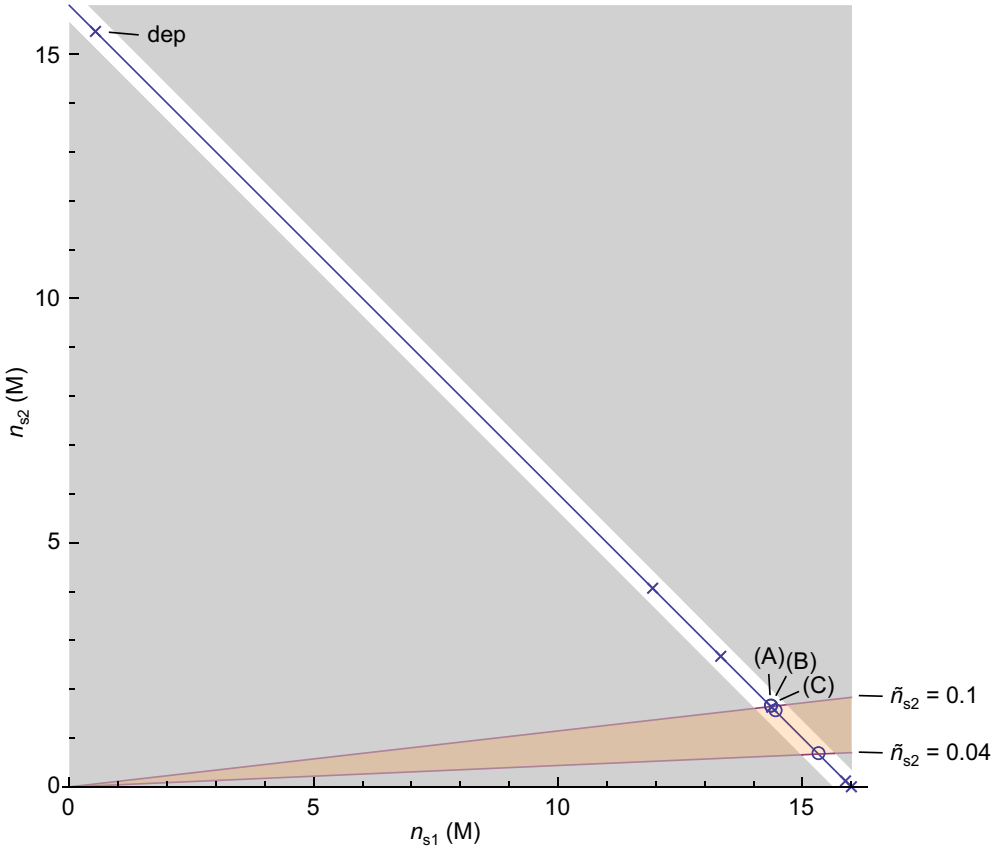

Supplementary Figure 2. Plot of experimental conditions with respect to the absolute surface concentrations of di- and monovalent cations, n_{s2} and n_{s1}. This plot shows that a particular value of $\tilde{n}_{s2}$ corresponds to exactly one surface condition, a particular pair of n_{s2} and n_{s1} values. The blue line indicates experimentally accessible pairs of n_{s2} and n_{s1} values for mica, given by the equation $n_s = n_{s1} + n_{s2} = 16\text{M}$—expressing our assumption that the total concentration of cations is constant. Gray shaded areas away from the blue line thus indicate that the paired n_{s2} and n_{s1} values at these points are impossible surface states for mica. Circles (O) denote experimental conditions with high lattice incorporation rates (> 90%); the remaining conditions (X) had significantly lower lattice incorporation rates. Red lines denote constant $\tilde{n}_{s2}$ values, in particular the two values for which we measured lattice incorporations >90%. Note two things. First, the experimental working regime is not the orange area between the two red lines, but rather the line segment between the intercepts of the red lines and the blue line. Second, all experimental conditions sharing a particular value of $\tilde{n}_{s2}$ (e.g. conditions (A), (B) and (C) with $\tilde{n}_{s2}$ of 0.1) all correspond to exactly the same surface cation condition at least in terms of estimated absolute surface concentrations of cations, e.g. a magnesium concentration of 1.6 M and a monovalent concentration of 14.4 M. "dep" indicates the condition for deposition of origami on mica.

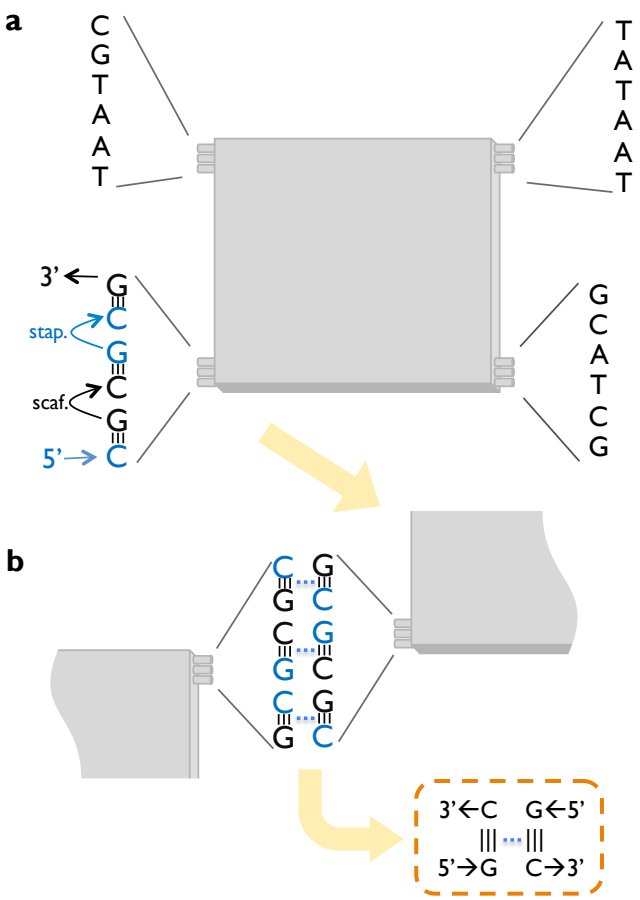

Supplementary Figure 3. Base sequences at blunt ends for the *N*=3 case. a, Base sequences at the four corners. One of the corners (the bottom left one in this diagram) had all 'GC' base pairs. Arrows indicate the 5'-3' directionality of scaffold and staple strands. The blue arrows and bases designate staple strands and the black ones designate the scaffold strand. The symbol '|||' indicates base pairing. (Arrow labeling, color-coding and pairing symbols are only applied to the bottom left corner, for simplicity). **b**, When the bottom left corner meets the same corner from another origami rectangle, they can form GC/CG stacks (shown in the dotted orange box), which have the strongest stacking free energy among all possible sequence pairs[6]. Before understanding the role of twist in checkerboard formation, we initially hypothesized that this diagonal bond might have formed preferentially and prevented the formation of linear chains (see main text for details).

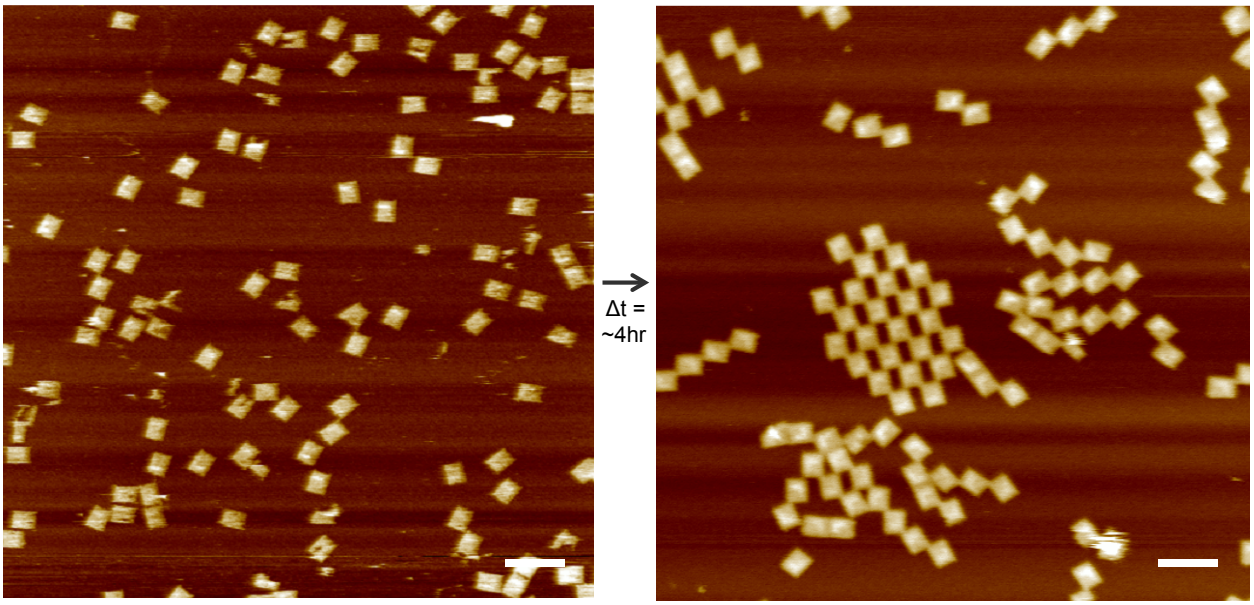

Supplementary Figure 4. AFM images of twisted, rectangular origami whose edge sequences were adjusted to be 'GC' at all four corners, before (left) and after (right) the surface diffusion protocol. Adjustment of the edge sequences to 'GC' was achieved based on a previously reported method[5]. Before the surface diffusion step, 'GC' rectangles did not form lattices or linear chains in solution (similar to twisted, non-GC rectangles). Our hypothesis had been that non-uniform stacking bond sequences were responsible for checkerboard formation. This would predict that after surface diffusion, 'GC'-rectangles would form many more linear chains than their non-'GC' counterparts. Instead, while some linear dimers formed, checkerboard lattices were predominantly observed. Scale bars: 300 nm.

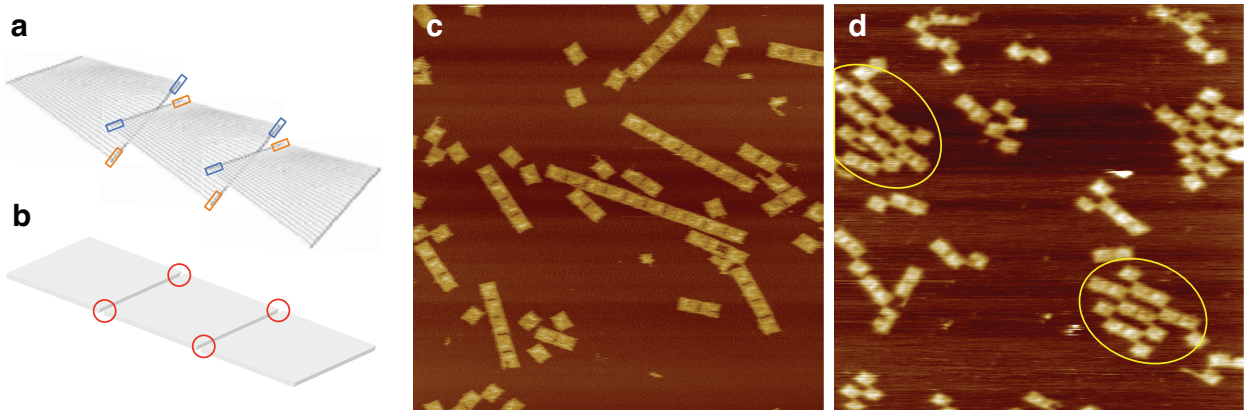

Supplementary Figure 5. Effect of origami twist. Models illustrate how origami twist might inhibit linear chain formation when constrained to a surface. **a**, For twisted origami, one pair of corners may bend up (blue boxes) while the other pair of corners (red boxes) bends down, causing a steric mismatch for linear assemblies. **b**, twist-free origami would not have such a steric mismatch. However, twisted origami are compatible with checkerboard lattice formation (see Supplementary Fig. 7a). **c**, Twist-reduced origami form linear chains in solution. **d**, After surface diffusion, some remain as linear chains, while some form checkerboards and others form double checkerboards (yellow ovals). These twist-reduced rectangles had 'GC' blunt ends. AFM images are 3 μm × 3 μm.

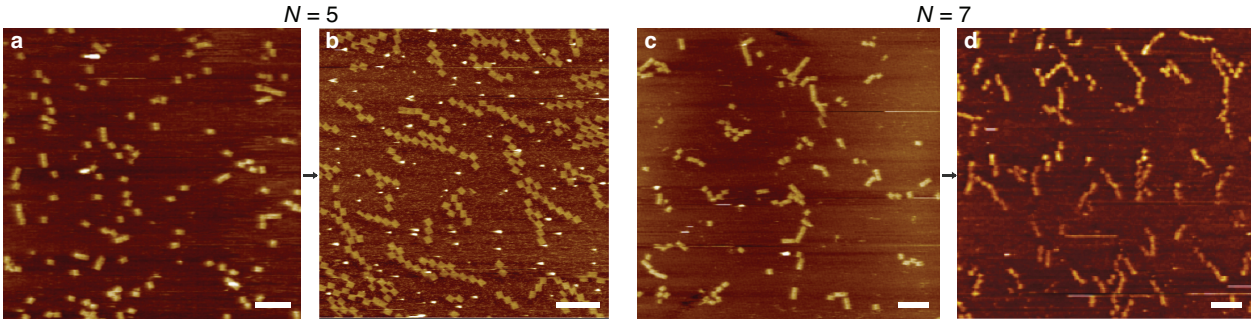

Supplementary Figure 6. Effect of stacking bond strength and size. a, N = 5, before surface diffusion: short linear chains form. **b,** N = 5, after surface diffusion: some checkerboard lattices form but diagonal chains dominate. **c,** N = 7, before surface diffusion: longer linear chains form than for N = 5. **d,** N = 7, after surface diffusion: a similar frequency of linear and diagonal chains suggests that less rearrangement occurs than for N = 5. Scale bars: 500 nm.

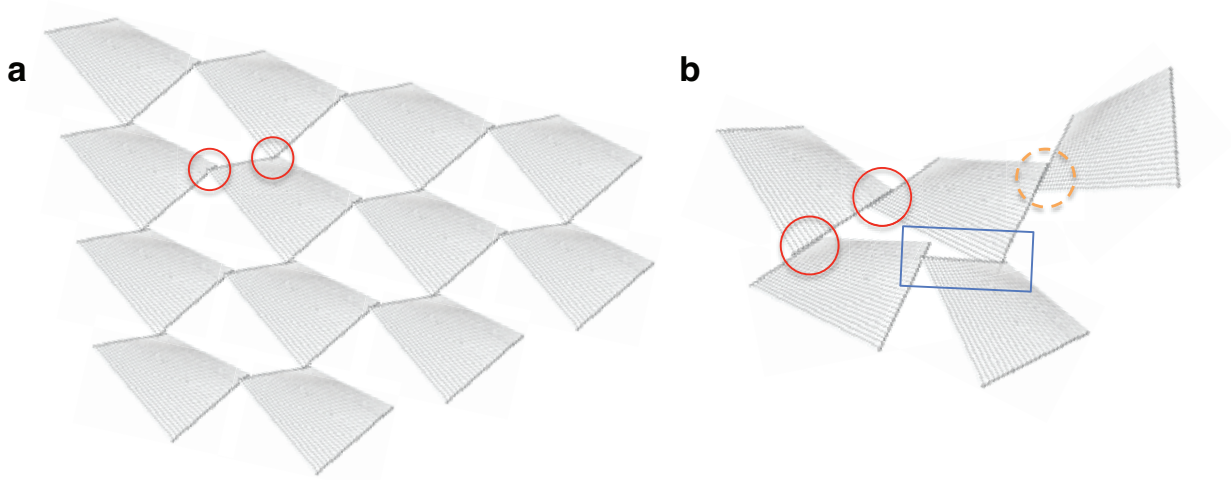

Supplementary Figure 7. Hypothetical effect of stacking bond size. a, With small overlap area for stacking bonds (e.g., 3 blunt ends), checkerboard bonds can form with minimal deformation on the edge geometry (two of which are indicated by red circles). **b,** With larger overlap area for stacking bonds (e.g., 7 blunt ends shown), bonds (red circles) guide the angles of next layer stacking patches, making checkerboard bonds hard to form (blue rectangle), while still allowing diagonal bonds to form (orange dotted circle).

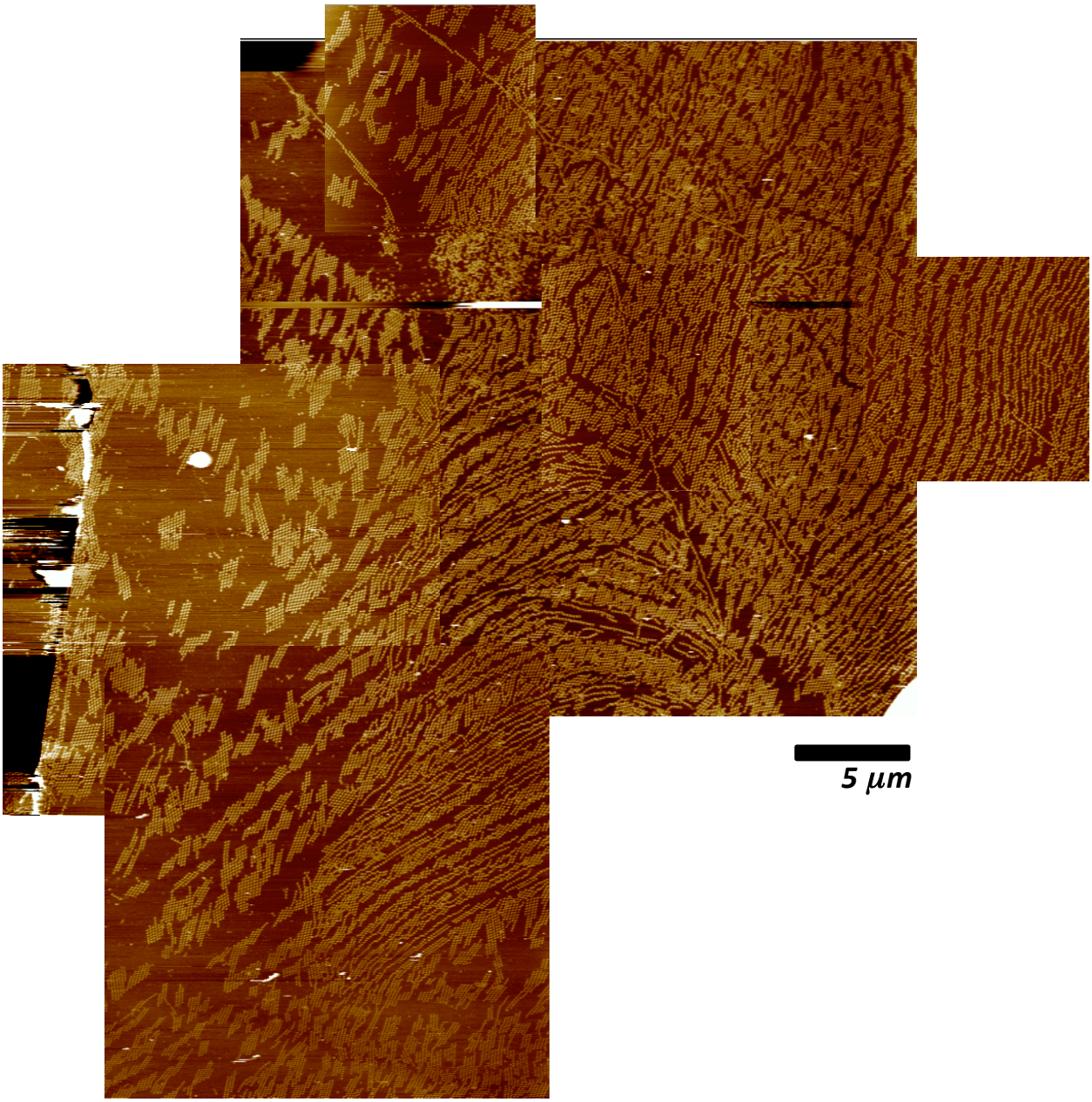

Supplementary Figure 8. A mosaic of AFM images that reveal correlations between checkerboard lattice size/shape and features of the mica surface. This figure is a wide-field view of the area shown in Figure 5 of the main text. For zoom-in views, see Figure 5. Quality control of mica cleaves is hard: at the left edge of the image mosaic, a large discontinuity in height is observed and it might have been used to identify this mica as a "bad cleave". In general, however, such features are difficult to detect by eye or optical microscope.

Supplementary Figure 9. Sequence and strand diagrams

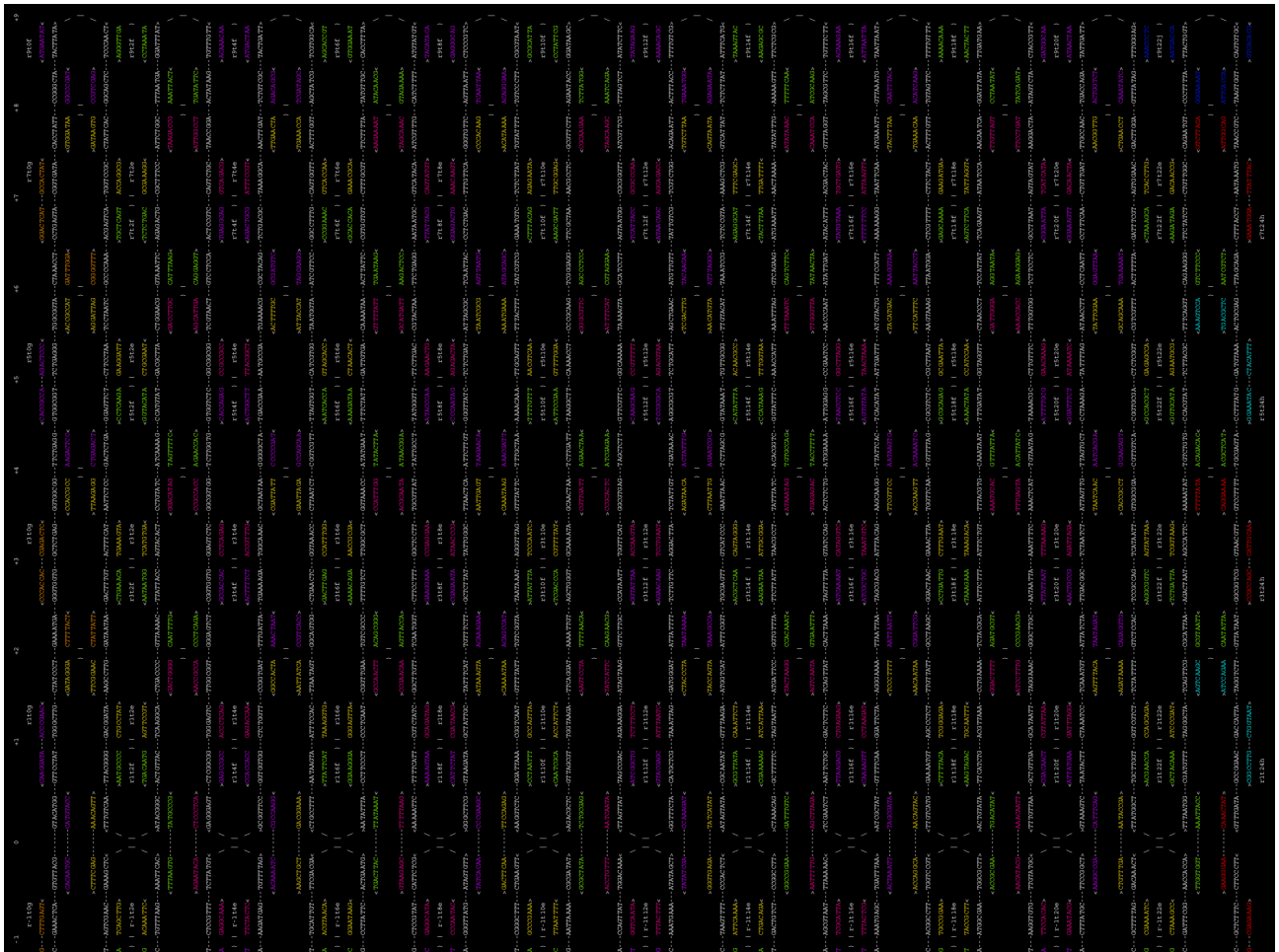

a, Sequence diagram for rectangle origami

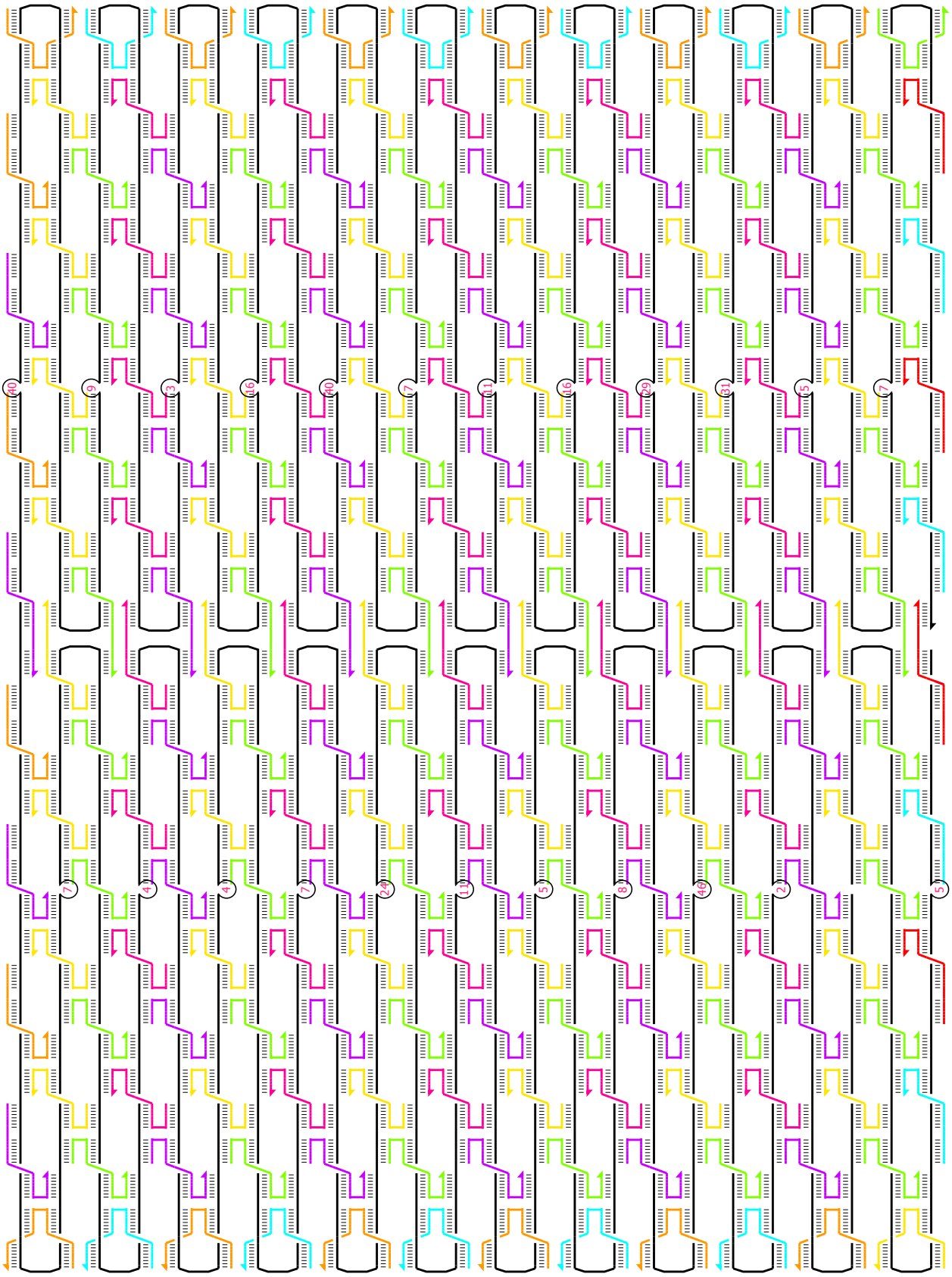

b, Strand diagram for rectangle origami with GC ends, with positions and lengths of loopouts (black circles with numbers) indicated; loopouts were introduced to generate ‘GC’ blunt-ends along the edges (see ref. 5 for details).

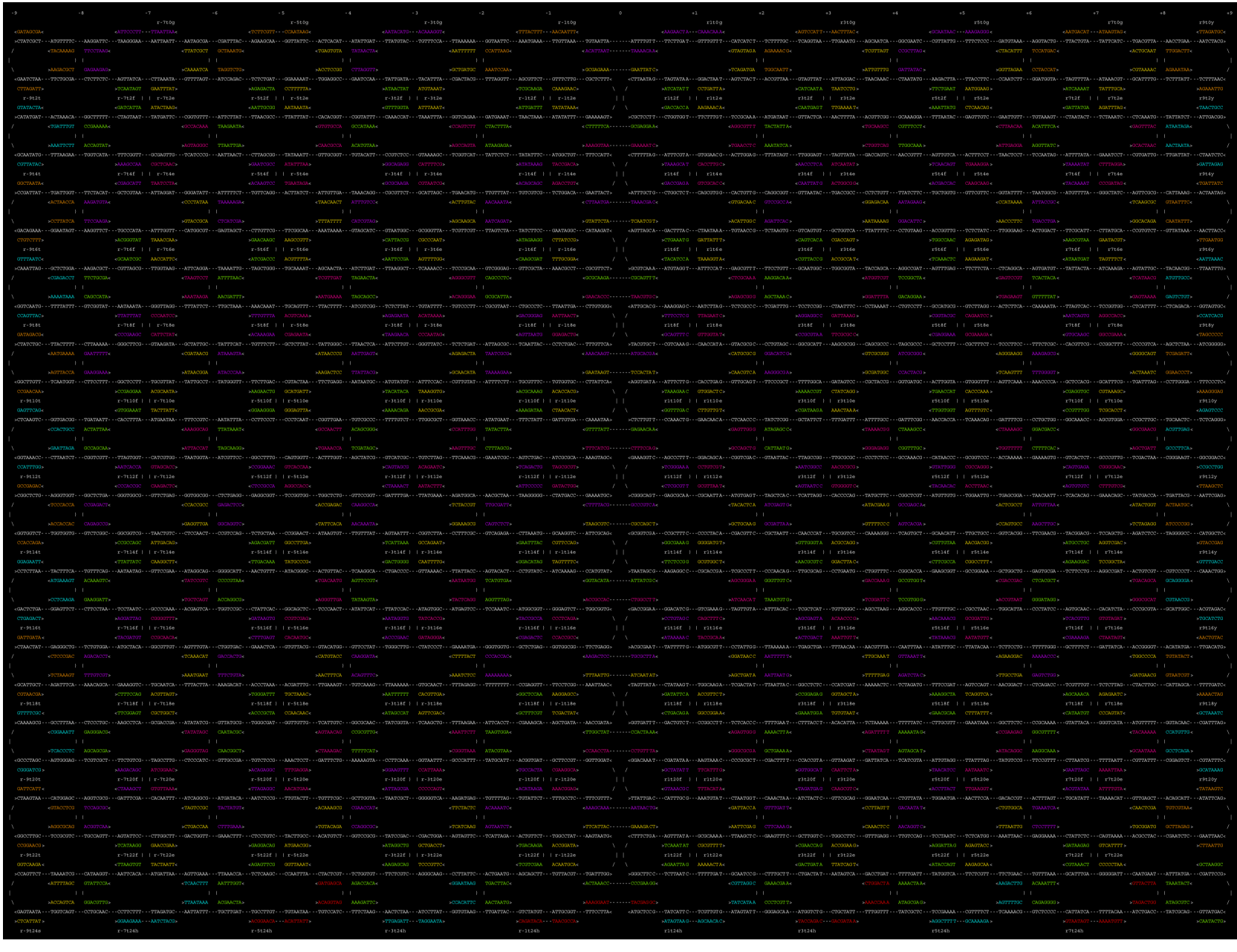

c, Sequence diagram for rectangle origami with GC ends

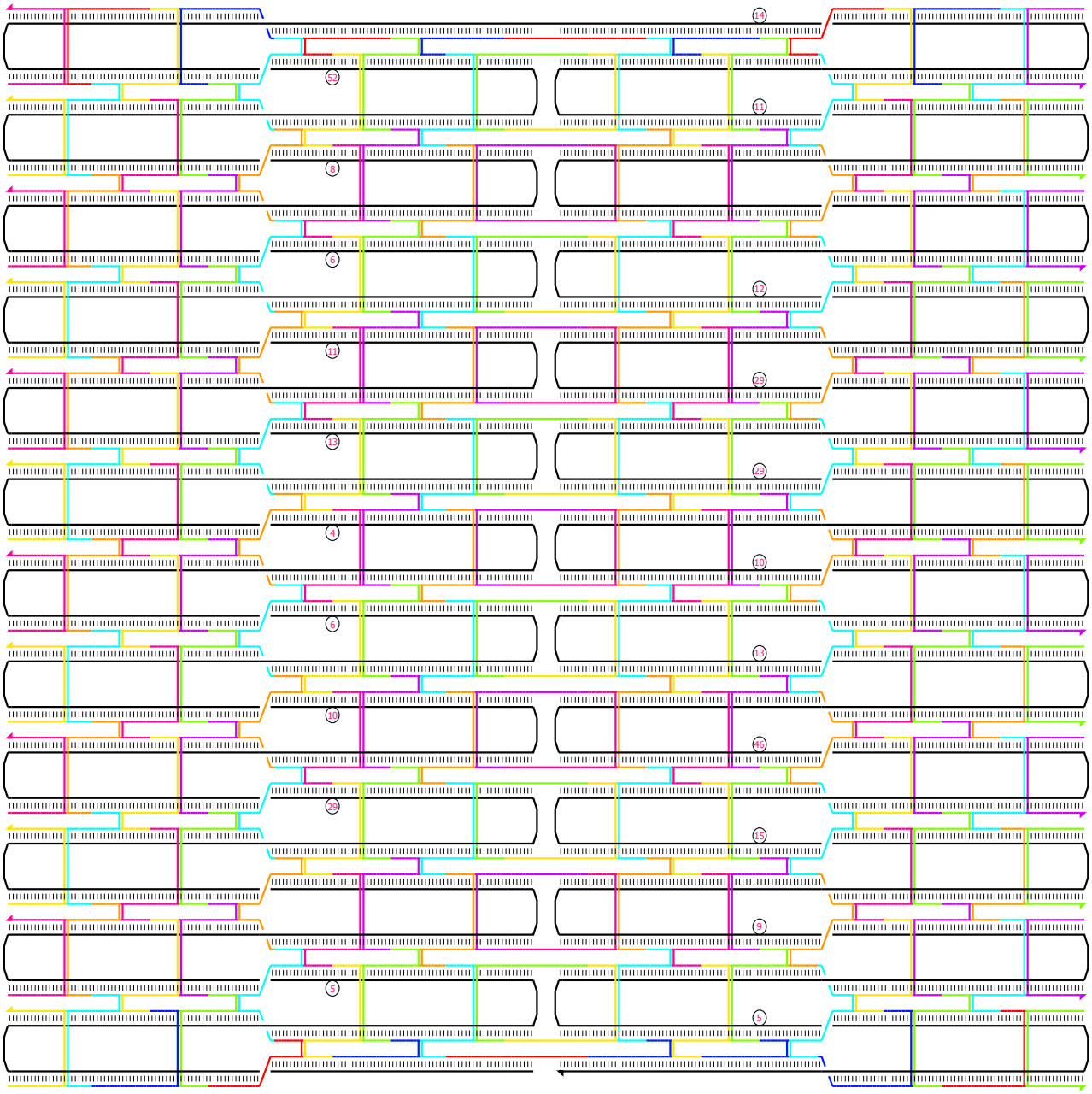

d, Strand diagram for rectangle origami with GC ends and reduced twist (10.44 bp/turn), with positions and lengths of loopouts (black circles with numbers) indicated; loopouts were introduced to generate ‘GC’ blunt-ends along the edges (see ref. 5 for details).

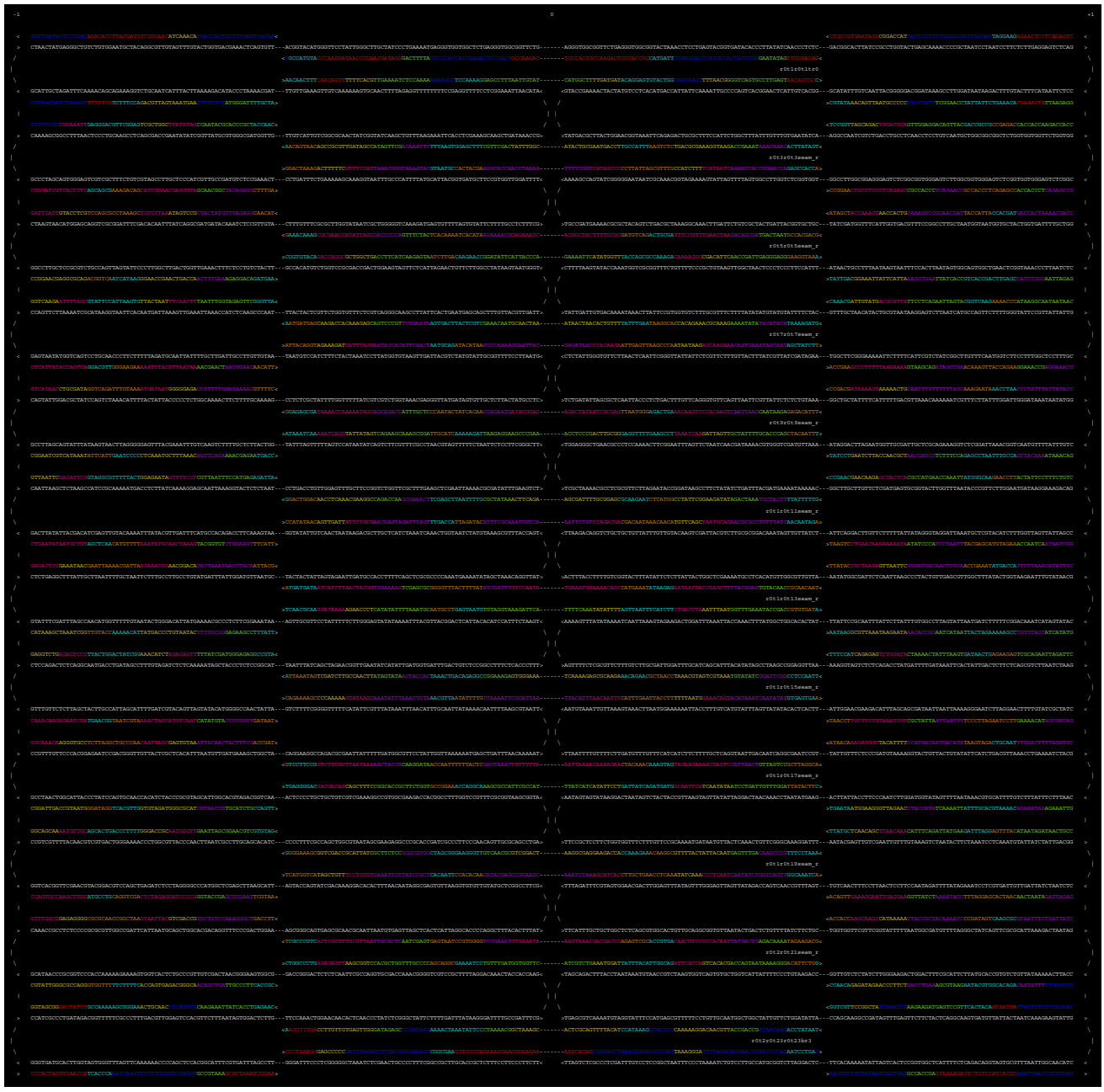

e, Sequence diagram for rectangle origami with GC ends and reduced twist (10.44 bp/turn)

Experimental condition	formal $[Mg^{2+}]$*	eff. $[Mg^{2+}]$*	$[Na^+]=[Cl^-]$*	eff. $[TrisH^+]$*	eff. $[CH3COO^-]$*	I*	$\varepsilon_r^{\#}$	λ_D (nm)	$\tilde{n}_{s2}$ on mica#	$\tilde{n}_{s2}$ on DNA#	$\tilde{n}_{b2}^{\#}$
Deposition (1× TAE/Mg^{2+})	12.5	11.5	0	14.6	64.98	62.79	78.41	1.21	0.97	0.95	0.44
$\tilde{n}_{s2}$=0 (NaCl only), Figure 4a	0	0	750	0	0	750	62.89	0.32	0	0	0
$\tilde{n}_{s2}$=0.007, Figure 4b	0.28	0.26	733.33	0.32	1.44	734.73	63.12	0.33	0.007	0.003	0.0003
$\tilde{n}_{s2}$=0.04†, Figure 4c	1.39	1.28	666.67	1.62	7.22	673.64	64.04	0.34	0.04	0.02	0.002
$\tilde{n}_{s2}$=0.1, Figure 4d	2.78	2.56	583.33	3.24	14.44	597.29	65.19	0.37	0.10	0.05	0.004
$\tilde{n}_{s2}$=0.17, Figure 4e	4.17	3.83	500	4.87	21.66	520.93	66.34	0.40	0.17	0.08	0.008
$\tilde{n}_{s2}$=0.25, Figure 4f	5.56	5.11	416.67	6.49	28.88	444.57	67.49	0.43	0.25	0.14	0.012
Add'l (A), $\tilde{n}_{s2}$=0.1, Figure 4g	5.56	5.11	793.53	6.49	28.88	821.43	62.29	0.31	0.10	0.05	0.006
Add'l (B), $\tilde{n}_{s2}$=0.1, Figure 4h	12.5	11.5	1,185.42	14.6	64.98	1,248.21	56.88	0.24	0.10	0.05	0.009
Add'l (C), $\tilde{n}_{s2}$=0.1, Figure 4i	0.28	0.26	179.68	0.32	1.44	181.08	70.76	0.70	0.10	0.05	0.001

Supplementary Table 1. Estimated values for the concentrations of all ionic species, ionic strength, the dielectric constant, the Debye length, and $\tilde{n}_{s2}$ values for mica and DNA for the solution conditions tested.

* All concentrations and ionic strengths are in units of mM.
# Dimensionless quantities.
† This experimental condition, with an $\tilde{n}_{s2}$ value of 0.04, was identical to that used for Step 2, the surface diffusion step, except that Step 2 was preceded by the deposition step, which could leave some Mg^{2+} adsorbed on the mica. This means that $\tilde{n}_{s2}$ might be slightly higher than 0.04 during the standard surface diffusion step.

Supplementary Note 1. Estimation of the concentrations of ionic species

For strong electrolytes such as NaCl and $Mg(CH_3COO)_2$ (magnesium acetate), we assumed full ionization. For example, 12.5 mM $Mg(CH_3COO)_2$ was assumed to yield 12.5 mM Mg^{2+} and 25 mM CH_3COO^-.

1× TAE/Mg^{2+} buffer contains 40 mM Tris acetate, 1 mM EDTA and 12.5 mM Mg^{2+} with pH 8.3. For Tris and acetate, we estimated the equilibrium concentrations based on their respective reactions with H^+ and their pKa values. First, for Tris, the following reaction

$$TrisH^+ \rightleftharpoons Tris + H^+$$

with pKa 8.06 at 25 °C was used to estimate the concentration of the cation $TrisH^+$. (Since $TrisH^+$ is a minor species in the system, compared to Na^+, the effect of temperature on the degree of ionization of $TrisH^+$ was neglected.) Because the formal concentration of Tris in 1× TAE/Mg^{2+} buffer is 40 mM and the pH is 8.3, we obtain the following relation, by letting $x = [TrisH^+]$,

$$Ka = 10^{-8.06} = \frac{[Tris][H^+]}{[TrisH^+]} = \frac{(40\text{-}x)\ 10^{-8.3}}{x}$$

and by solving for x, we get $[TrisH^+]$ = 14.6 mM. Likewise, for CH_3COO^- we use the following reaction

$$CH_3COOH \rightleftharpoons CH_3COO^- + H^+$$

for which the pKa value is 4.76. We used a formal concentration of 65 mM (25 mM from magnesium acetate and 40 mM from TAE buffer), and from the equilibrium relation, we get $[CH_3COO^-]$ = 64.98 mM.

For Mg^{2+} ions, since EDTA (1 mM) contained in the TAE/Mg^{2+} buffer can chelate Mg^{2+} ions with high affinity ($K_{eq} = 10^{8.7}$), we assumed the effective concentration of Mg^{2+} to be the formal concentration of Mg^{2+} less the concentration of EDTA.

The estimated concentrations for all ions under all experimental conditions are summarized in Supplementary Table 1.

Supplementary Note 2. Estimation of Debye lengths

The Debye length of an ionic solution is given by the following relation:

$$\lambda_D = \sqrt{\frac{\varepsilon_r \varepsilon_0 k_B T}{2 N_A e^2 I}} \quad \textbf{(1)}$$

where ε_r is the dielectric constant of the solution, ε_0 is the vacuum permittivity, k_B is Boltzmann's constant, T is the absolute temperature, N_A is Avogadro's number, e is the elementary charge, and I is the ionic strength defined by:

$$I = \frac{1}{2}\sum_{i=1}^{n} c_i z_i^2 \quad \textbf{(2)}$$

where c_i is the concentration of the ion i, z_i is the charge number of the ion, and the sum is taken over all ionic species in the solution. The ionic strengths and the Debye lengths of solutions under different experimental conditions were calculated based on the concentrations estimated above, and are listed in Supplementary Table 1.

The dielectric constant of an aqueous solution is dependent on the temperature and the ionic strength. The dielectric constant decreases with increasing temperature (a solution becomes less polarizable with increased kinetic energy of the water molecules) and also decreases with increasing ionic strength (a solution becomes less polarizable when ions trap water molecules in specific orientations; this is called the 'dielectric decrement'[1]). We assume that the effects of temperature and ionic strength on the dielectric constant of water are independent of each other and simply add the effects linearly. First, the dependence of the dielectric constant of water on temperature is given by the following relation[2]:

$$\varepsilon_r\,(\mathrm{T}) = 0.24921\times10^{3} - 0.79069\ \mathrm{T} + 0.72997\times10^{-3}\ \mathrm{T}^2. \quad \textbf{(3)}$$

The effect of ions is only considered for NaCl, because the effect of the overall ionic strength on the dielectric constant is not well understood, to the best of our knowledge, and Na^+ and Cl^- were the major ionic species for most conditions while all other ions had relatively low (<0.1 M) concentrations. The effect of NaCl on the dielectric constant of water can be considered linear[1] for [NaCl] ≤ ~1 M, and the correction term is given by -γ[NaCl], where γ is 13.8 M^{-1} for NaCl. Estimates of the dielectric constant combining both the effects of temperature and ionic strength are summarized in Supplementary Table 1.

Supplementary Note 3. Calculation of $\tilde{n}_{s2}$ values

$\tilde{n}_{s2,}$ the fractional surface density of Mg^{2+} under different solution conditions was calculated using the equations introduced in the main text. One can solve the resulting quadratic equation for $\tilde{n}_{s2}$ which yields:

$$\tilde{n}_{s2} = \frac{(2Y+1)-\sqrt{(4Y+1)}}{2Y} \quad \textbf{(4)}$$

$$\text{where } Y = n_{b2} \times n_s / n_{b1}^2. \quad \textbf{(5)}$$

For the bulk concentrations of divalent and monovalent cations, n_{b2} and n_{b1}, we used their effective concentrations as estimated in the section above. For monovalent cations, we summed the concentrations of Na^+ and $TrisH^+$. Values of n_s, the total surface concentration of cations, for mica (16 M) and DNA (6.65 M) were adopted from ref. 3 and ref. 4 which estimated them from the surface charge densities for mica and DNA, under the assumption that the total charge density and the total surface concentration of cations are constant for the given surface, and are independent of the bulk concentrations of the cations (assumptions of "counterion condensation theory"); n_s values are the same whether monovalent or divalent cations are considered because the volume used for calculating the concentration is defined by a characteristic distance from the surface (λ_z) at which a cation's electric potential energy equals the thermal energy[4] which is dependent on cation valence z. Potential minute effects of temperature and the dielectric constant on n_s values were ignored and n_s values were treated as constant for a given surface. Different surfaces have different n_s values which yield different $\tilde{n}_{s2}$ values for a given experimental condition. In the main text, we used $\tilde{n}_{s2}$ values calculated for mica when discussing the critical conditions for surface diffusion and lattice incorporation, but all of our arguments work equally well with $\tilde{n}_{s2}$ values calculated for DNA. Ref. 3 uses $\tilde{n}_{s2}$ calculated for DNA; for purposes of comparison, the working regime in terms of $\tilde{n}_{s2}$ for DNA is 0.02-0.05. Note that since n_s values are constant, equivalent working regimes can be found for the absolute divalent cation surface concentration n_{s2} for either DNA or mica. Alternatively, as will be discussed in the next section, one can use the expression n_{b2}/n_{b1}^2 as a surface-independent parameter for describing the working regime.

The calculated values of $\tilde{n}_{s2}$ for mica and DNA under all experimental conditions are listed in Supplementary Table 1.

Supplementary Note 4. $\tilde{n}_{s2}$ is the parameter which best correlates with lattice-formation.

Given the experimental evidence and theoretical justifications for $\tilde{n}_{s2}$ as a determinant of strong-to-weak DNA-mica binding transitions, we examined whether lattice incorporation rates reflected this for a variety of values of $\tilde{n}_{s2.}$ (Figure 4a-g of the main text. Lattices were defined to be clusters containing more than one origami, in the checkerboard configuration.) Rather than finding a simple relationship, like a single critical value for $\tilde{n}_{s2}$ below which lattice incorporation rates were high, we found an apparent peak centered around $\tilde{n}_{s2}$ values of 0.04 and 0.1 (Supplementary Fig. 1a, top), where lattice incorporation rates were greater than 90%. We declared values of $\tilde{n}_{s2}$ in the range 0.04 and 0.1 to be a "working regime" for lattice formation, presuming that they would have similarly high lattice incorporation rates. It was possible that a different ionic parameter might have a simpler correlation with lattice formation (e.g. perhaps a single critical value, or even a linear relationship with lattice incorporation rates) and so we plotted lattice incorporation rates as a function of bulk magnesium concentration, $[Mg^{2+}]$, monovalent cation concentration $[mono^{+}]$, bulk fraction of divalent cations, $\tilde{n}_{b2}$, ionic strength I, and Debye length λ_D (top plots of Supplementary Fig. 1b-f). No single critical values emerged. Instead a single peak appeared in plots for all of the parameters, and thus all six parameters were equivalent with respect to defining similar continuous working regimes (pink shaded areas in Supplementary Fig. 1 top plots, e.g. bulk Mg^{2+} concentration between 1.28 and 2.56 mM, or I between 0.597 and 0.674 mM).

To explore the hypothesis that $\tilde{n}_{s2}$ might still best correlate with lattice formation, we carried out experiments for three additional conditions all of which had the same $\tilde{n}_{s2}$ value (0.1) which fell within the working regime, but which had very different bulk concentrations of Mg^{2+} and monovalent cations (conditions (A), (B), and (C); details listed in Supplementary Table 1). We added lattice incorporation rates for these conditions to the top plots of each panel of Supplementary Fig. 1 to create the bottom plots of each panel in Supplementary Fig. 1. As can be seen in the bottom plot of Supplementary Fig. 1a for $\tilde{n}_{s2}$, both conditions (A) and (B) have lattice incorporation rates >90% which allow our original definition of working regime to be preserved. Condition (C) showed extremely low lattice incorporation rate inconsistent with the working regime. We justify this by observing that condition (C)'s ionic strength is particularly low (and its Debye length particularly high) which are consistent with particularly strong binding due to ion correlations (see Supplementary Fig. 1e,f, bottom).

All other parameters correlate less well with lattice formation. Bulk magnesium concentration correlates the worst since, with the addition of conditions (A) and (B) there exist two magnesium concentrations for which both excellent (>90 %) and poor (20% or less) lattice incorporation is observed (marked by a diagonally striped pattern in the bottom of Supplementary Fig. 1b). For all other parameters ($[mono^{+}]$, $\tilde{n}_{b2}$, I, and λ_D) no continuous working regime can be constructed, because at least one experimental condition with a lattice incorporation rate significantly less than 90% falls between pairs of conditions with lattice incorporation rates greater than 90% (Supplementary Fig. 1c-f, bottom).

To help understand the relationships between important ionic parameters, cation concentrations, and lattice incorporation rates, we plotted our experimental conditions with respect to the bulk concentrations of divalent and monovalent cations (an n_{b2}-n_{b1} plot, Figure 4l of the main text) and with respect to the surface concentration of divalents and monovalent cations (an n_{s2}-n_{s1} plot, Supplementary Fig. 2).

Figure 4l of the main text does two things: (1) It helps differentiate which parameter, the surface fraction of divalents ($\tilde{n}_{s2}$) or the bulk fraction of divalents ($\tilde{n}_{b2}$) best correlates with the working regime for

lattice formation. (2) It shows the region for which we believe $\tilde{n}_{s2}$ breaks down as a predictor of lattice formation, namely high Debye length (λ_D).

Red contours of constant $\tilde{n}_{s2}$ (for $\tilde{n}_{s2}$ = 0.1 and 0.04) and are given by the quadratic equation:

$$n_{b2} = n_{b1}^2 \times \tilde{n}_{s2} / \{(1- \tilde{n}_{s2})^2 \times n_s\}. \quad \textbf{(6)}$$

Blue contours of constant $\tilde{n}_{b2}$ (for $\tilde{n}_{b2}$ = 0.006 and 0.002) and are given by the linear equation:

$$n_{b2} = n_{b1} \times \tilde{n}_{b2} / (1- \tilde{n}_{b2}). \quad \textbf{(7)}$$

We note that if one wishes to characterize the lattice-forming regime without considering inferred or difficult-to-measure surface properties of the mica surface (such as the surface cation concentration n_s) and think in only terms of bulk solution parameters [Mg^{2+}] and [$mono^+$], then the red parabolas can equivalently be parameterized as curves of constant $n_{b2}/n_{b1}^2 = [Mg^{2+}]/[mono^+]^2$, and then the blue lines are most comparably parameterized by just their slope, $n_{b2}/n_{b1} = [Mg^{2+}]/[mono^+]$. But, as Supplementary Fig. 2 shows, we think this point of view misses an important physical picture introduced by the use of $\tilde{n}_{s2}$. In Figure 4l of the main text, the orange shaded area indicates that a single continuous range of $\tilde{n}_{s2}$ values best captures the working regime; it fails only for a single experimental condition with a high Debye length (C). The blue shaded area and blue dotted line demonstrate that no single continuous range of $\tilde{n}_{b2}$ values can capture the working regime because a single condition (#) with significantly lower lattice incorporation rate (<70%) falls between them.

Gray contours of constant λ_D are shown for $\lambda_D \approx 1$ and 0.6 nm. Ignoring small potential variations of the dielectric constant as a function of temperature and ionic strength (see discussion in Supplementary Note 2) and considering only major ionic species (Mg^{2+}, Na^+ and Cl^-) the gray lines are given by the equation:

$$n_{b2} = -1/2 \times n_{b1} + 1/2 \times I, \quad \textbf{(8)}$$

where I can be calculated from λ_D by equation (1) in Supplementary Note 2. Note that while condition (C) has an $\tilde{n}_{s2}$ value of 0.1, it has a λ_D = 0.70 nm which we suggest results in strong ion correlations that prevent surface diffusion and subsequent lattice formation. Note that the deposition condition has a λ_D of 1.21 nm.

While $\tilde{n}_{s2}$ is defined as the fractional surface density of divalent cations, this definition is somewhat deceiving in that it obscures the relationship of $\tilde{n}_{s2}$ to the state of absolute cation concentrations on the surface. Consider the space of all possible surface concentrations for divalent (n_{s2}) and monovalent (n_{s1}) cations (Supplementary Fig. 2). One might naively think that because contours of constant $\tilde{n}_{s2}$ are lines in this space, that an $\tilde{n}_{s2}$ of a particular value would mean that the absolute surface concentration of cations could assume values corresponding to any point on that line. Two such lines are plotted in red (shown for $\tilde{n}_{s2}$ = 0.1 and $\tilde{n}_{s2}$ = 0.04) and given by the equation:

$$n_{s2} = n_{s1} \times \tilde{n}_{s2} / (1- \tilde{n}_{s2}). \quad \textbf{(9)}$$

However, the assumption that the surface is strongly ionizing and has a constant concentration of cations (n_s = 16 M for mica) limits allowable values of n_{s2} and n_{s1} to occur on the line (blue in Supplementary Fig. 2) given by:

$$n_s = n_{s1} + n_{s2} = 16 \text{ M}. \quad \textbf{(10)}$$

Thus each value of $\tilde{n}_{s2}$ corresponds to a single particular pair of concentrations—curves of constant $\tilde{n}_{s2}$ in Figure 4l of the main text, which represent very different bulk cation concentrations, actually correspond to exactly one surface cation condition. This is why we think parameterizing these curves by $[Mg^{2+}]/[mono^{+}]^2$, while convenient, obscures a physically important interpretation of these curves. Reporting $\tilde{n}_{s2}$, however, is not enough. In general, given a highly ionizable surface, and other assumptions made here, critical values of $\tilde{n}_{s2}$ for a phenomenon should always be reported in a way that emphasizes the assumed or observed value of n_s. This is important because if an estimate of n_s changes later, because of, say, a new observation, $\tilde{n}_{s2}$ values for a particular phenomena's critical values will have to be recalculated because of their dependence on n_s (whereas reported $[Mg^{2+}]/[mono^{+}]^2$ would not have to be); see the dependence of $\tilde{n}_{s2}$ on n_s in Supplementary Equations (4) and (5). Alternatively, one could simply report both absolute surface concentrations of cations, (n_{s1}, n_{s2}), which makes n_s obvious. Either way, reporting ($\tilde{n}_{s2}$, n_s) or (n_{s1}, n_{s2}) satisfactorily captures the idea that a large number of bulk solution conditions collapse to a single surface condition.

Supplementary Note 5. Stacking bond strength as a function of ionic conditions

A central assumption of this work is that the extent of origami surface diffusion, as a function of ionic conditions, is what determines the lattice incorporation rates that are observed. The idea is that low surface diffusion rates yield lower lattice incorporation, and that high surface diffusion rates yield higher lattice incorporation. *A priori,* an alternative hypothesis involving the strength of stacking bonds seems plausible. In particular, one might imagine that the strength of stacking bonds changes sharply with a change in ionic conditions: conditions which decrease stacking bond strength could result in low lattice incorporation, and conditions which increase stacking bond strength would result in high lattice incorporation. Thus it is important to consider this hypothesis.

To explore the "changing bond strength" hypothesis we conducted a series of additional experiments to measure the strength of stacking bonds under various solution conditions, in particular for those conditions that exhibited lower lattice incorporation rates. This included the condition (C), which has both the lowest Mg^{2+} concentration and a low Na^{+} concentration, and might be expected to yield a very low stacking bond strength. To separate the influence of surface diffusion from the strength of stacking bonds, we measured the strength of stacking in the context of solution-based experiments developed in our previous work[5]. Briefly, the energy of stacking bonds were measured based on monomer-dimer equilibrium for an origami rectangle with blunt ends on only one side, by counting the population of monomers and dimers in AFM images of an equilibrated solution sample and estimating the respective concentrations. For tests under various solution conditions, we used the same basic rectangle design used elsewhere in this study, but with 24 blunt ends on the right-hand side of each origami rectangle. We decided to use 24 blunt ends to ensure a significant occurrence of dimerization because, as we have noted elsewhere in the paper, 6 blunt ends (3 at each corner) do not induce measurable dimerization.

We measured stacking bond strength for the following four conditions:
(a) Condition (C), corresponding to Fig. 4i with I = 181 mM.
(b) The deposition condition (12.5 mM Mg^{2+}) corresponding to Fig. 3b with I = 63 mM.
(c) The NaCl-only condition, corresponding to Fig. 4a with I = 750 mM.
(d) The standard diffusion condition as a control with I = 674 mM.

Note that (a) and (b) represent the conditions with the lowest ionic strengths and the worst performance in terms of lattice incorporation (near 0%). (c) represents the Mg^{2+}-free condition that exhibited a moderate lattice incorporation rate (65%) with a small average lattice size (~3), and has the highest ionic strength (except for the two extreme additional conditions (A) and (B) with n_{s2}=0.1 which showed superior lattice formation).

We found that under the two worst-performing conditions, the strength of stacking bonds were indeed weaker than the control condition, but only mildly: measured binding energies were lower by ~12.2% for (a) (-0.585 kcal/mol for a pair of stacking blunt ends) and by ~7.7% for (b) (-0.615 kcal/mol) when compared to the control (d) (-0.666 kcal/mol). For condition (c), the bond turned out to be ~0.7% stronger (-0.670 kcal/mol). Thus our best hypothesis for poor lattice formation remains that poor surface diffusion of origami prevents high lattice incorporation rates.

Supplementary Note 6. Effects of blunt-end sequence and origami twist

Because the origami rectangles were designed with the potential for stacking bonds at each of their four corners, they are compatible with the formation of structures with two different basic geometries: (1) the two-dimensional checkerboard lattice discussed so far and (2) one-dimensional linear chains (Supplementary Fig. 5b). An origami in either of these geometries is attached to its neighbors by four bonds, and so, the two structures should have roughly the same thermodynamic stability. A 2D lattice does have more unsatisfied bonds at its edges than a 1D chain does at its ends, and lattices might exhibit nucleation barriers to their crystallization, whereas linear chains should not. Thus, *a priori*, one might expect the products of rectangle assembly to include a significant fraction, if not a preponderance, of linear chains. Experimentally, no linear chains were observed and, surprisingly, numerous seemingly less favorable diagonal chains (a single origami wide) with the same bonding pattern as checkerboard lattices, but half as many bonds per tile were observed.

Our initial hypothesis was that the bias towards the lattice-type bonding pattern might be attributable to the non-uniform sequences of the bases at the blunt ends of potential stacking bonds. The binding energy of the stacking interaction has a strong dependence on the base sequences of the blunt ends[6,7]. Thus despite the apparent symmetry of the rectangles, different pairs of corners may have a greater or lesser affinity for each other. When we examined the blunt-end sequences at each corner, we found that one corner was indeed rich in 'GC' (see Supplementary Fig. 3). This corner, when bound to itself between two rectangles occurring with a 180◦ rotated orientation (1) would give the highest stabilization[7] and yield the strongest possible stacking bond of all possible pairs of bonded corners and (2) is an example of the lattice-type bonding pattern. Thus during the assembly step, such bonds might form first, and bias the remaining corners to make lattice-type bonds. To test whether non-uniform blunt-end sequences might be creating a bias towards lattices, we designed a rectangle with a single sequence ('GC') at all blunt ends, as described previously[5]. When subjected to surface diffusion, these rectangles behaved similarly to those with nonuniform sequences, depositing as monomers and predominantly forming checkerboard lattices with a few linear dimers (Supplementary Fig. 4). This led us to ask whether origami structure, rather than sequence, might explain the bias towards lattices.

In fact, the original origami rectangle design[8] was found to have a significant global twist[5,9,10] in solution due to the fact that it was designed with 10.67 base pairs per turn, rather than 10.4–10.5 base pairs per turn. By AFM, highly twisted DNA origami appear flat, both in the strongly immobilizing regime of Step 1, and the surface diffusion regime of Step 2. This is unsurprising since only origami which are strongly bound to the surface can be imaged stably, and any structures that are not tightly adhered are imaged as smears, or are invisible. The hypothesis then is that rectangles which are mobile during Step 2, those which are involved in bonding and growth of structures, are not entirely flat and that two of their corners are somewhat lifted off of the mica surface. These corners, which occur along the diagonal of the rectangle, may inhibit linear chain formation by causing a steric mismatch (Supplementary Fig. 5a) but they may not inhibit the formation of lattices (Supplementary Fig. 7a).

To test this hypothesis, we used an origami rectangle with reduced global twist, described previously[5], with the idea that they would be able to form chains as in Supplementary Fig. 5b. Interestingly, imaging of reduced-twist rectangles at Step 1 shows that they form long linear chains in solution (Supplementary Fig. 5c), which was never observed using the original, highly-twisted origami. This suggests that the original rectangles do not form chain structures in solution because their edges are so distorted that the

binding energy of the stacking bonds (involving 6 helices) cannot overcome the distortion. (Original rectangles with stronger 24-helix stacking bonds can overcome this distortion and form highly-twisted linear chains in solution[5].)

After Step 2 (Supplementary Fig. 5d), a mixture of checkerboard lattices, linear chains, and a new double-checkerboard lattice (indicated by yellow ovals) whose repeat unit is a linear dimer were observed. The observation that checkerboard and double-checkerboard lattices dominate after surface diffusion clearly shows that the long linear chains formed in solution at least partially break and rearrange during the surface diffusion. Understanding whether the observed distribution of structures simply reflects the relative kinetics of lattice-type and chain-type bonds when the rectangles are confined to the surface, or whether the twist-reduced origami have residual twist which still favors lattices would require future study. Nevertheless, the observation of linear chains of twist-reduced origami upon deposition, and mixed structures after surface diffusion, strongly support the idea that twist of the original rectangles is responsible both for their initial deposition as monomers, and their subsequent formation of checkerboard lattices.

Supplementary Note 7. Effects of the stacking bond strength and size

Increasing the number of blunt ends participating in each stacking bond both increases the strength of the stacking bond[5] and changes the size and geometry of the bond. While our original experiments with $N = 3$ blunt ends per bond yielded high lattice incorporation rates, it was unclear whether this choice was optimal for lattice formation. Thus we additionally tested $N = 5$ and $N = 7$ blunt ends per bond.

Again, AFM after initial deposition served to give a picture of solution structures. As the number of blunt ends increased, so did the tendency for rectangles to form linear chains (Supplementary Fig. 6a,c). This is consistent with the idea that stronger stacking bonds can better overcome the distortion in highly-twisted rectangles.

After surface diffusion, some rectangles remained in linear chains, but a large fraction of rectangles were incorporated into checkerboards and diagonal chains (Supplementary Fig. 6b,d). We make several observations. First, both the $N = 5$ bonds and to a lesser extent the $N = 7$ bonds were still weak enough to allow rearrangement under our diffusion protocol. Second, on the surface, the stronger bonds still could not overcome the steric effects due to twist, and the rearranged structure have lattice-type bonds rather than forming linear chains. Third, and most interesting, is that the structures which dominate as N is increased are diagonal chains, as can be most clearly seen in Supplementary Fig. 6b. We attribute this to the high twist of the origami rectangles, in combination with the increased size of the stacking bonds. Stacking bonds provide a geometric constraint between the edges of two origami, aligning their helices and setting the angle between them. For lattices to grow, they must be able to bind highly-twisted origami at certain edge sites which require the formation of two simultaneous bonds. For stacking bonds of three helices, it appears that an incident rectangle and its bonding partners are able to bend sufficiently to allow growth (Supplementary Fig. 7a). For larger stacking bonds of five or seven helices, it appears that the geometry enforced by the stacking bonds requires greater bending to allow an incident rectangle to form two bonds (Supplementary Fig. 7b, blue rectangle). Thus while such larger bonds can easily support the growth of diagonal chains (Supplementary Fig. 7b, orange dotted circle), they cannot as easily form checkerboard lattices.

Supplementary References

1 Levy, A., Andelman, D. & Orland, H. Dielectric constant of ionic solutions: A field-theory approach. *Phys. Rev. Lett.* **108**, 227801 (2012).

2 Wohlfarth, C. "Permittivity (dielectric constant) of liquids," in *CRC Handbook of Chemistry and Physics, 94th Edition (Internet Version 2014)*, W. M. Haynes, ed., CRC Press/Taylor and Francis, 2013.

3 Pastré, D. *et al.* Adsorption of DNA to mica mediated by divalent counterions: A theoretical and experimental study. *Biophys. J.* **85**, 2507-2518 (2003).

4 Rouzina, I. & Bloomfield, V. A. Competitive electrostatic binding of charged ligands to polyelectrolytes: Planar and cylindrical geometries. *J. Phys. Chem.* **100**, 4292-4304 (1996).

5 Woo, S. & Rothemund, P. W. K. Programmable molecular recognition based on the geometry of DNA nanostructures. *Nature Chem.* **3**, 620-627 (2011).

6 Protozanova, E., Yakovchuk, P. & Frank-Kamenetskii, M. D. Stacked-unstacked equilibrium at the nick site of DNA. *J. Mol. Biol.* **342**, 775-785 (2004).

7 Yakovchuk, P., Protozanova, E. & Frank-Kamenetskii, M. D. Base-stacking and base-pairing contributions into thermal stability of the DNA double helix. *Nucleic Acids Res.* **34**, 564-574 (2006).

8 Rothemund, P. W. K. Folding DNA to create nanoscale shapes and patterns. *Nature* **440**, 297-302 (2006).

9 Dietz, H., Douglas, S. M. & Shih, W. M. Folding DNA into twisted and curved nanoscale shapes. *Science* **325**, 725-730 (2009).

10 Ke, Y. *et al.* Multilayer DNA origami packed on a square lattice. *J. Am. Chem. Soc.* **131**, 15903-15908 (2009).